A FRAMEWORK FOR NUMERICAL FLOW SIMULATION OF THE ROTOR BLADE WITH AEROELASTIC DEFORMATION USING THE MODEL DEFORMATION MEASUREMENT DATA

Kohei KONISHI
Tokyo University of Agriculture and Technology
Tokyo, Japan

Kosuke SAITO
Tokyo University of Agriculture and Technology
Tokyo, Japan

Masato IMAI
Tokyo University of Agriculture and Technology
Tokyo, Japan

Hideaki SUGAWARA
Japan Aerospace Exploration Agency
Tokyo, Japan

Yasutada TANABE
Japan Aerospace Exploration Agency
Tokyo, Japan

Kazuyuki NAKAKITA
Japan Aerospace Exploration Agency
Tokyo, Japan

Masaharu KAMEDA
Tokyo University of Agriculture and Technology
Tokyo, Japan

ABSTRACT

Coupled CFD/CSD methods are widely used for the efficient development of rotorcraft incorporating aeroelasticity, but validation with wind tunnel testing has revealed significant discrepancies between these coupled simulations and experiments. These discrepancies may arise from uncertainties in the CFD and/or CSD components. However, it is difficult to identify the exact cause of these discrepancies solely through coupled simulations. In this study, we developed a numerical method to account for aeroelastic deformation using model deformation measurement (MDM) data, without relying on structural properties. We outlined a method for reconstructing the deformed shape of rotor blades using MDM data and demonstrated its effectiveness with data obtained from wind tunnel tests. The reconstructed shape was highly accurate, with errors of less than 0.3 mm. CFD simulations were subsequently conducted using the deformations obtained through the developed method, revealing differences in time-averaged aerodynamic loads and vibration behavior depending on whether elastic deformation was accounted for or not.

INTRODUCTION

The fluid-structure interaction (FSI) of rotor blades is important in the prediction of the overall rotorcraft performances, the safety assessment of the rotor system, and the noise induced by the blade vortex interaction (BVI). The rotor blades are so high-aspect-ratio airfoils that aeroelasticity strongly affects their aerodynamic performance. With the recent development of computer technology, coupled methodologies of computational fluid dynamics (CFD) and computational structural dynamics (CSD) are widely used for numerical simulation of aeroelastic problems (Refs. 1–4).

For accurate analysis of such aeroelastic phenomena, it is important to improve the accuracy of both structural parameters such as stiffness and mass distribution that contribute to elastic deformation of the blade, and fluid modeling including turbulence and transition models. In order to improve the accuracy of pure CFD, efforts are being made internationally to validate CFD through detailed comparisons of flow fields obtained from CFD and wind tunnel tests, and to accumulate best practices for accurate simulation (Refs. 5, 6).

On the other hand, the CFD/CSD coupling simulations for helicopter blades reviewed in (Ref. 3) indicate that further investigations are needed to obtain consensus on the prediction capabilities of CFD and CSD methods even though the blade deformation predicted from CFD/CSD coupling simulations fairly agrees with the HART-II experiments. Jung et al. (Ref. 7) measured the structural properties of the HART-II blade and found certain discrepancies between the predicted and the actual value, particularly regarding the location of the center of gravity (CG). They also reported that changing the CG location introduces discrepancies in aeroelastic twist predictions. From the above, more precise assessments of CFD and CSD are required to improve the prediction accuracy. In particular, simulating the actual deformation in the numerical simulation accurately is critical for evaluating the CFD capabilities in moving objects, such as helicopter blades.

A method for reconstructing the deformed shape of the entire wing from the data of strain gauges attached to the wing surface has been proposed (Ref. 8). However, this method is less desirable for comparison with CFD as attaching strain gauges to the model surface changes its shape. On the other hand, model deformation measurement (MDM) is a non-contact method to measure the deformed shape of a model using multiple cameras (Refs. 9, 10). In particular, the method using stereo digital image correlation (stereo-DIC) (Ref. 10) can measure complex deformation shapes with high spatial resolution. However, the optical method using cameras cannot measure the deformation shape of the entire blade because it can only measure the deformation of the blade surface that can be captured by the camera. For example, if the upper surface of the blade is measured, the lower surface, which is in the blind spot of the camera, cannot be measured at the same time.

This study aims to develop a method to reconstruct the deformation shape of the entire blade using the deformation measurement data obtained by a stereo DIC technique. This paper describes the blade deformation geometry reconstruction method proposed in the study and shows the results of applying the method to the helicopter blade test data. CFD simulation is also performed using the deformation shapes obtained by the proposed method to simulate deformation conditions equivalent to those in wind tunnel tests, and the results are also presented.

WIND TUNNEL TEST

The experimental data used in this paper were acquired during the wind tunnel test held at the Low-Speed Wind Tunnel (LWT2) in Japan Aerospace Exploration Agency (JAXA) Chofu Aerospace Center. The test model is the helicopter model developed by JAXA, as shown in Figure 1. The rotor blade made of CFRP is a scaled model equivalent to the main rotor blade of the UH-60A. The blade radius is 765 mm.

The test condition referred to in this paper is listed in Table 1. The collective and cyclic blade pitch angles are determined by the following equation.

$$\theta(\psi) = \theta_0 + \theta_{1c}\cos\psi + \theta_{1s}\sin\psi \tag{1}$$

The cyclic blade pitch θ_{1c}, θ_{1s} are adjusted so that the total moments around each axis are balanced.

Model Deformation Measurement

The deformation of the rotor blade is acquired by the stereo-DIC. The setup for the deformation measurement is shown in Figure 2. The optical system consists of two high-resolution cameras (Prosilica GX6600, Allied Vision Technologies) and five LED illuminators (IL-106, HARDsoft Microprocessor Systems) are mounted on the rotation stage. By rotating the rotation state, the blade deformation data at any measurement azimuth angle is acquired. The shooting timing are determined by the incremental rotary encoder (UN1000, MUTOH). The measurement frequency is about 1 Hz. The spatial resolution of the image for MDM is about 0.12 mm/pixel. At the same time, six-component forces and moments applied to the rotor system except for the fuselage are also acquired by the six-component balance. In this study, the captured images are processed using VIC-3D 8 (Correlated Solutions Inc.), a commercial software for stereo-DIC.

The deformation measurement data from stereo-DIC is point cloud data representing the target object surface. The deformation measurement data consists of one set of data at rest and during deformation occured, which are called "ref" and "run" respectively in this paper. The i-th ref point is denoted by $\boldsymbol{p}_i$ and the i-th run point is denoted by $\boldsymbol{p}'_i$. $\boldsymbol{p}_i$ and $\boldsymbol{p}'_i$ are the measured points before and after deformation at the same location on the blade surface.

Figure 1: Helicopter test model in the JAXA LWT2

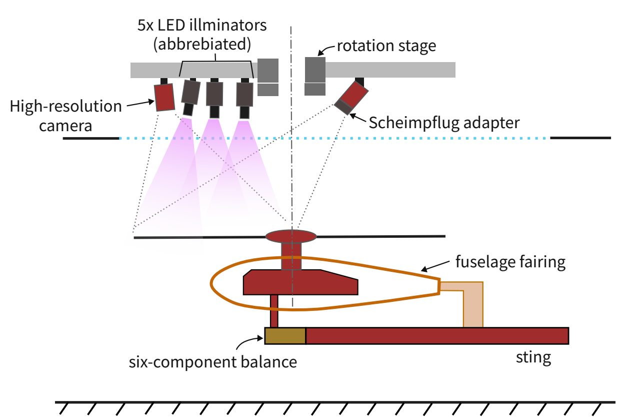

Figure 2: Schematic diagram of the wind tunnel test setup for the MDM

MODEL DEFORMATION RECONSTRUCTION

This section describes the present method to reconstruct the geometry of the deformed model. Figure 3 shows the overview of the procedure of the proposed method.

Definition of the Model Parameters

The present method assumes the slender body, like a wing, to allow the deformation of the body can be approximated by three deformation modes, inplane bending, antiplane bending, and twist. A geometric model shown in Figure 4 is considered in order to reduce the dimension of the model parameters. Each element is orthogonal to the ref-curve. The inplane and antiplane bending is represented by the deflection of the ref-curve, and the twist is represented by the rigid rotation of each element around the cross point with the ref-curve. The two-dimensional profile of each cross-section element is represented by the polyline, and the body surface is represented by the triangle mesh by connecting nodes on the neighbor elements as shown in Figure 6.

In the present method, the deformation is expressed by the following polynomial function, on the analogy of the Eular-Bernoulli elastica.

$$\Delta x(s) = \sum_{i=0}^{N_b} \alpha_i s^i, \quad \Delta z(s) = \sum_{i=0}^{N_b} \beta_i s^i, \quad \Delta\phi(s) = \sum_{i=0}^{N_\phi} \gamma_i s^i \tag{2}$$

where N_b and N_ϕ are the degrees of the polynomial of the bending and the twist deformation respectively. Each coefficients in the polynomial are the model parameters, and putting the vector $\boldsymbol{x} = \left(\alpha_0 \dots \alpha_{N_b}\ \beta_0 \dots \beta_{N_b}\ \gamma_0 \dots \gamma_{N_\phi}\right)^T$, which called ”deformation parameter” in this paper. The method for identifying the deformation parameters is described in the next section.

Table 1: Flow condition

rotor speed	940 rpm
mainstream velocity	30.1 m/s
advance ratio μ	0.4
collective pitch θ_0	7.87°
lateral cyclic pitch θ_{1c}	−8.52°
longitude cyclic pitch θ_{1s}	1.52°

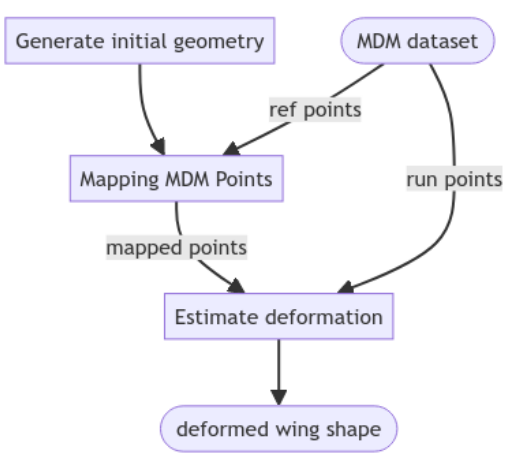

Figure 3: Overview procedure of the reconstruction method

The deflection of the ref-curve is determined based on the displacement vector $\boldsymbol{d}(s) = (\Delta x(s)\ 0\ \Delta z(s))^T$ and the spanwise displacement to preserve the total spanwise length. The ref-curve after deformation $\boldsymbol{l}'$ is obtained by the following step. First, the ref-curve is divided into N_c segments. Then, the ref-curve after the deformation can be obtained from the wing root by the following equation.

$$\boldsymbol{l}' = \begin{cases} \boldsymbol{l}(0) + \boldsymbol{d}(0) & i = 0 \\ \boldsymbol{l}'_{i-1} + \dfrac{\|\boldsymbol{l}(s_i) - \boldsymbol{l}(s_{i-1})\|}{\|\boldsymbol{v}\|}\boldsymbol{v} & i \neq 0 \end{cases} \tag{3}$$

$$\boldsymbol{v} = \boldsymbol{l}(s_i) + \boldsymbol{d}(s) - \boldsymbol{l}'_{i-1} \tag{4}$$

And finally, the coordinate on the deformed ref-curve $\boldsymbol{l}'(s)$ at an arbitrary spanwise position s is obtained by interpolating the point obtained in equation 3 with the cubic spline curve.

The movement of each element is determined by the twist deformation and the ref-curve deflection The normal vector $\boldsymbol{n}(s)$ associated with the element at the spanwise position s, shown in the figure 5, is obtained as follows,

$$\boldsymbol{n}(s) = \frac{\mathrm{d}\boldsymbol{l}(s)}{\mathrm{d}s} \Big/ \left\| \frac{\mathrm{d}\boldsymbol{l}(s)}{\mathrm{d}s} \right\| \tag{5}$$

The basis vectors of the wing element $\boldsymbol{\xi}(s)$, $\boldsymbol{\eta}(s)$ at the spanwise position s are defined as follows,

$$\boldsymbol{\xi}(s) = R(\varphi, \boldsymbol{n}_b)\boldsymbol{e}_x \qquad \boldsymbol{\eta}(s) = R(\varphi_b, \boldsymbol{n}_b)\boldsymbol{e}_z \tag{6}$$

$$\varphi_b(s) = \arccos(\langle \boldsymbol{n}(s), \boldsymbol{e}_y \rangle) \tag{7}$$

$$\boldsymbol{n}_b(s) = \boldsymbol{e}_y \times \boldsymbol{n}(s) \tag{8}$$

where $R(\varphi, \boldsymbol{n})$ represents the representation matrix of rotation φ around the axis $\boldsymbol{n}$. $\boldsymbol{e}_x$, $\boldsymbol{e}_y$ and $\boldsymbol{e}_z$ are unit vectors along with x, y, z axis in the global coordinate system respectively.

Identification of the deformation parameter

The deformation parameter $\boldsymbol{x}$ is identified by solving the following non-linear minimization problem.

$$\boldsymbol{x} = \arg\min_{\boldsymbol{x}} E(\boldsymbol{x}) \tag{9}$$

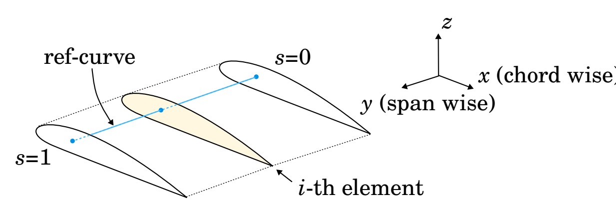

Figure 4: Wing geometric model

where $E(\boldsymbol{x})$ is an error between the identified geometric model and the run point cloud.

MDM can obtain the point cloud of the surface of the target but it is not clear to which position on the target surface each point corresponds. When estimating the deformation parameters, it is necessary to evaluate the error between the measured point cloud and the estimated geometric model. However, the calculation of the distance between a point and a surface is computationally expensive and unsuitable in terms of processing time. Thus, a map point cloud is created by projecting the ref point cloud to the target shape model as shown in Figure 7, and the distance between the map point cloud and the run point cloud is taken as the error $E(\boldsymbol{x})$. The error can be expressed as follows,

$$E(\boldsymbol{x}) = \sum_{i=0}^{N} \left\| \boldsymbol{p}' - P_{\boldsymbol{p}_i,\boldsymbol{x}_0}(\boldsymbol{x}) \right\| \tag{10}$$

where N is the number of measurement points, $\boldsymbol{p}'$ is a i-th run point, $\boldsymbol{p}_i$ is an i-th ref point, $\boldsymbol{x}_0$ is an initial deformation parameters, and $P_{\boldsymbol{p}_i,\boldsymbol{x}_0}(\boldsymbol{x})$ is the position of the point generated by projecting $\boldsymbol{p}_i$ onto the wing surface at $\boldsymbol{x} = \boldsymbol{x}_0$ when the deformation parameter is $\boldsymbol{x}$ The details about the map point $P_{\boldsymbol{p}_i,\boldsymbol{x}_0}(\boldsymbol{x})$ are described in the next section.

Derivation of the Map Points

The map point cloud is obtained based on the procedure shown in Algorithm 1. Each variable in the Algorithm 1 is illustrated in Figure 8 and defined as following equations.

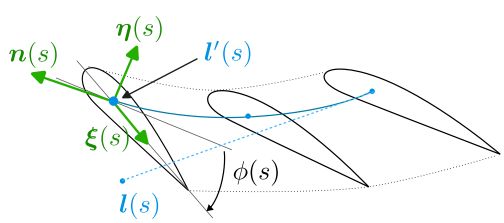

Figure 5: Definition of the element coordinate system

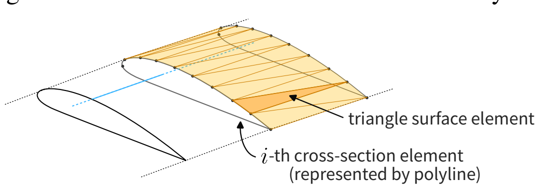

Figure 6: Schematic diagram of the surface meshing

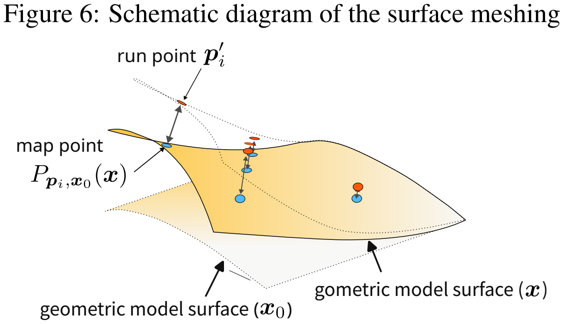

Figure 7: Schematic diagram of the map points and the error calculation

Algorithm 1 Derivation of map points Q

Input: P: ref points, S: list of triangle mesh elements
Output: Q: A list of tuples containing map points and their corresponding element numbers

```
for p_i ∈ P do
    S_n ← n nearest neighbors to p_i among S
    for p_i ∈ P do
        m_i ← a point projected P_i to the surface of s_k along e_z direction.
        if s_k includes m_i then
            q_i ← convert m_i into k-th local coordinate system
            Q ← Q ∪ (k, q_i)
            break
        end if
    end for
end for
return Q
```

$$\boldsymbol{m}_i = \boldsymbol{p}_i + \frac{\langle \boldsymbol{o}_k(\boldsymbol{x}), \boldsymbol{n}(\boldsymbol{x}_0)\rangle - \langle \boldsymbol{p}_i, \boldsymbol{n}(\boldsymbol{x}_0)\rangle}{\langle \boldsymbol{n}(\boldsymbol{x}_0), \boldsymbol{e}_z\rangle} \boldsymbol{e}_z \tag{11}$$

$$\boldsymbol{q}_i = [U_k^T(\boldsymbol{x}_0) U_k(\boldsymbol{x}_0)]^{-1} U_k^T(\boldsymbol{x}_0)(\boldsymbol{m}_i - \boldsymbol{o}_k(\boldsymbol{x}_0)) \tag{12}$$

$$U_k(\boldsymbol{x}) = [\boldsymbol{u}_k(\boldsymbol{x}) \; \boldsymbol{v}_k(\boldsymbol{x})] \in \mathbb{R}^{3\times 2} \tag{13}$$

where blacket $\langle \cdot, \cdot \rangle$ represents the inner product of two vectors, $\boldsymbol{m}_i$ is a coordinate point projected ref point $\boldsymbol{p}_i$ to the k-th mesh element along with the z-axis, $\boldsymbol{q}_i \in \mathbb{R}^2$ is a location at the local coordinate system corresponding to the mesh element to which $\boldsymbol{m}_i$ is projected.

As described above, representing the map point cloud as the local coordinate systems on the target surface, the map point at an arbitrary deformation parameter $\boldsymbol{x}$ can be expressed as follows.

$$P_{\boldsymbol{p}_i,\boldsymbol{x}_0}(\boldsymbol{x}) = U_k(\boldsymbol{x})\boldsymbol{q}_i + \boldsymbol{o}_k(\boldsymbol{x}) \tag{14}$$

Initial Reconstruction

The high aspect-ratio structure, such as the helicopter blade used in this study, produces large deformation downwards due to gravity. If $\boldsymbol{x}_0 = \boldsymbol{0}$ is used as the initial deformation parameters, a quite discrepancy arises between the initial geometric model and the geometry represented by the ref point cloud. Therefore, in the present method, the initial deformation shape is estimated in advance of the estimation of the aeroelastic deformation.

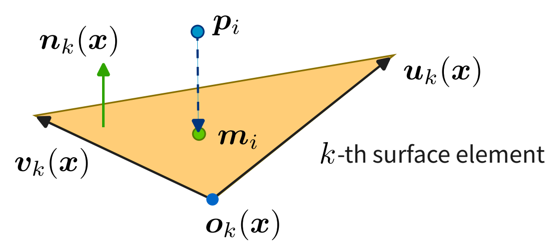

Figure 8: Definition of the local coordinate system of the k-th surface element

In this paper, for simplicity, the initial deformation can be assumed by the z-axis component only. As shown in Figure 9, a point cloud projected onto the geometry expressed by $\boldsymbol{x} = 0$ is generated. Then, the initial deformation parameter $\boldsymbol{x}_0$ is obtained by solving the following equation to minimize the error between the point cloud $P_{\boldsymbol{p}_i,0}(\boldsymbol{x})$ and the ref point cloud,

$$\boldsymbol{x}_0 = \arg\min_{\boldsymbol{x}} \sum_{i=0}^{N} \left\| \boldsymbol{p} - P_{\boldsymbol{p}_i,\boldsymbol{0}}(\boldsymbol{x}) \right\|. \tag{15}$$

Deformation Parameters at an Arbitrary Azimuth

A deformation parameter at an arbitrary azimuth angle is obtained by the following procedure. First, the MDM is taken for multiple azimuth angles $\psi_0, \psi_1, \ldots$, and the presented method is applied to each measurement data to obtain the deformation parameters $\boldsymbol{x}_{\psi_0}, \boldsymbol{x}_{\psi_1}, \ldots$ at each azimuth. Then, the discrete Fourier transformation (DFT) is applied to each deformation parameter. Finally, a deformation parameter at an arbitrary azimuth angle ψ is obtained by the following Fourier series.

$$\boldsymbol{x}(\psi) = \sum \left[\boldsymbol{a}_k \cos(k\psi) + \boldsymbol{b}_k \sin(k\psi) \right] \tag{16}$$

where $\boldsymbol{a}_k$ and $\boldsymbol{b}_k$ are the Fourier coefficients calculated by the DFT.

RECONSTRUCTION OF HELICOPTER BLADE DEFORMATION

Conditions

The constant terms for bending deformation in equation 2 are set to $\alpha_0 = \beta_0 = 0$ because the blade roots are supported by the pin fixation. The constant term for twist deformation in equation 2 is set to the blade pitch angle calculated by the equation 1. The degree of the polynomial for bending deformation is set to $N_b = 4$ with reference to the Eular elastica, and the degree of the polynomial for the twist is set to $N_\phi = 4$ to ensure freedom in shape representation. The minimization problem defined in Equations 9, equation 15 are solved using Levenberg-Marquardt iterative method. The number of measurement points for each MDM data used in this paper was about 1.6 million points.

Results

Figure 10 shows the error between the reconstructed initial deformation geometry and the ref point cloud acquired by the MDM. The error in the figure is the shortest Euclidean distance from each ref point to the reconstructed blade surface. This represents the accuracy of the initial reconstruction described in the previous section. Blank regions in the Figure 10 are caused by the failure of the stereo-DIC processing due to the reflection of the LED light at the surface of the blade.

The standard deviation of the error between the reconstructed initial geometry and the ref point cloud is 0.32 mm. The initial reconstruction is achieved with an accuracy of less than 0.3 mm over almost the entire area of the blade. At the root of the blade, the error is increased rather than the other area. This error is considered to be caused by errors from MDM measurements due to bokeh of images used for stereo-DIC, and errors between blade pitch angles assumed in the blade geometry reconstruction and the actual blade pitch angle in the wind tunnel test. Improvement is expected by precisely measuring the blade pitch angle in the wind tunnel test and reflecting it in the boundary conditions of the proposed method.

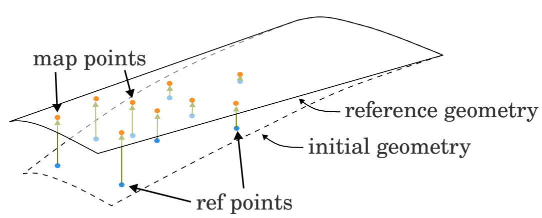

Figure 9: Mapping ref points to the reference geometry for initial deformation reconstruction

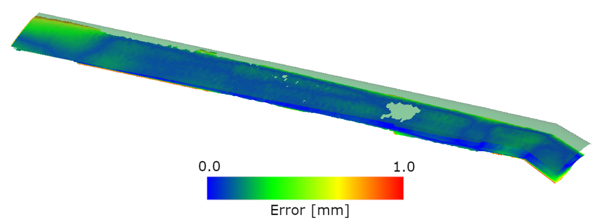

(a) error distribution (shaded object is reference geometry)

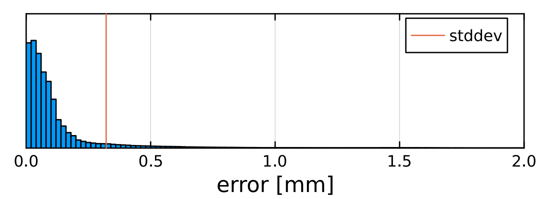

(b) histogram of the initial reconstruction error

Figure 10: Error distribution of the initial deformation shape reconstruction

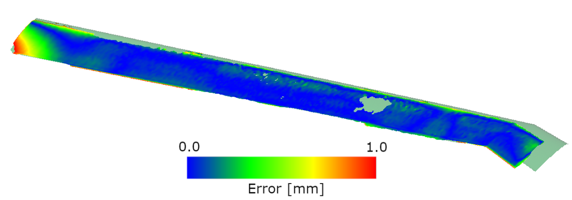

(a) error distribution (shaded object is reference geometry)

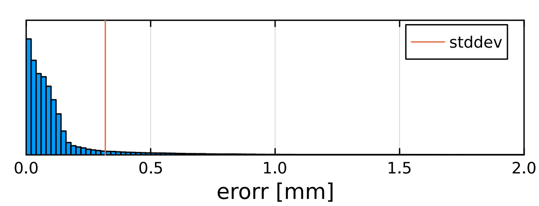

(b) histogram of the reconstruction error

Figure 11: Error distribution of the deformation shape reconstruction

Figure 11 shows the error between the reconstructed deformation geometry and the run point cloud acquired by the MDM. The standard deviation of the error is 0.32 mm. As initial geometry reconstruction, the error is increased around the blade root. This is considered to be caused by slight deformation of the pitch link due to the aerodynamic loads applied on the blade, and errors from MDM measurements due to bokeh of images used for stereo-DIC. Assuming the blade chord length is about 50 mm, the error in blade pitch is roughly about 1 degree calculated from the errors at the blade root. However, the overall reconstruction of the blade deformation is reasonable because the error except for the blade root region, which lessly contributed to the rotor performances, is within the 0.3 mm or less.

Figure 12 shows the blade tip deformation ($s = 1$) for each azimuth angle. The scatter points in the figure show the blade tip deformation calculated from the deformation parameters $\boldsymbol{x}_{\phi_0}, \boldsymbol{x}_{\phi_1}, \ldots$ for each measurement azimuth angle. The curves in the figure show the blade tip deformation from the DFT using the estimated parameters $\boldsymbol{x}_{\phi_0}, \boldsymbol{x}_{\phi_1}, \ldots$. The CFD simulation reproducing the deformation in the wind tunnel test is carried out in the next section using these Fourier coefficients.

CFD SIMULATION

This section describes the CFD simulation imposing the transient deformation shape obtained by the present reconstruction method. The compressible moving overset CFD code, rFlow3D, developed by JAXA is used for the CFD simulation. The computational grid consists of outer and inner background, blade, and fuselage grids as shown in Figure 13. Table 2 shows the number of each grid. The length of the side of the outer background grid is $200R$.

Table 3 lists the numerical schemes and turbulent and transition models used in this simulation. The rotor speed is 940 rpm, the freestream velocity $U_\infty = 30.1\,\mathrm{m/s}$, the freestream temperature $T_\infty = 291.7\,\mathrm{K}$, which conform to the flow condition in the wind tunnel test.

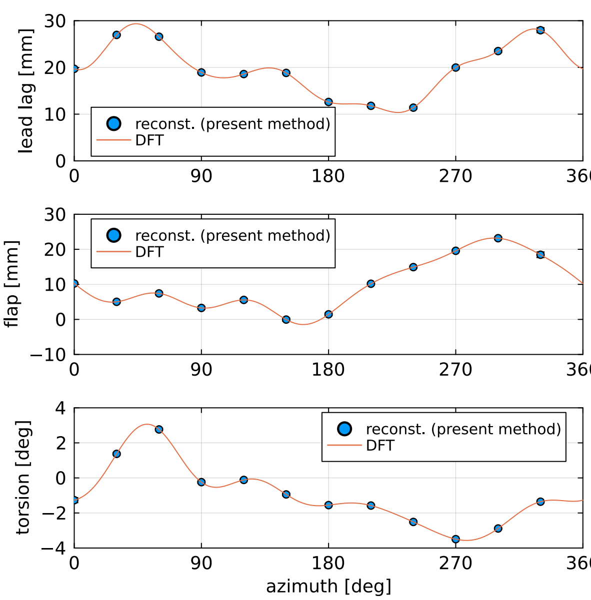

Figure 12: Blade tip deformation for each azimuth angle

Two cases, 1 and 2, are defined in order to assess the influence of the aeroelastic deformation of the rotor blade. Case 1 takes into account the aeroelastic deformation of the rotor blade using the present method. For this case, the blade pitch angle is set to the pitch angle measured in the wind tunnel test. Case 2 uses the rigid blade. For this case, the collective pitch angle is set as same as in case 1, but the cyclic pitch angle is set so that the total moment is balanced using the trim analysis feature implemented in the rFlow3D.

CFD RESULT

Table 4, shows the average of one rotation of the thrust and the torque coefficients obtained by CFD and the time-averaged coefficients acquired during the wind tunnel test. Comparing the aerodynamic coefficients with the wind tunnel test results, the coefficients are underestimated when aeroelastic deformation is considered, and the errors with 2.9% for C_T and 13.2% for C_Q in case 1. Without considering the deformation, the coefficients overestimates and the errors are 1.8% for C_T and 13.9% for C_Q.

Table 2: Number of grids

	# of grids
outer background grid	$115 \times 119 \times 119$
inner background grid	$331 \times 249 \times 129$
blade grids	$153 \times 125 \times 71$
fuselage grid	$106 \times 101 \times 71$

Table 3: Numerical schemes and models

Grid type	Background	Body
Higher-order scheme	FCMT (Ref. 11)	
Advection term	modified SLAU (Ref. 12)	
Time integration	4-stage RK	LU-SGS
Turbulence model	k-ω SST (SST-2003)	
Transition model	γ-$\mathrm{Re}_{\theta t}$	

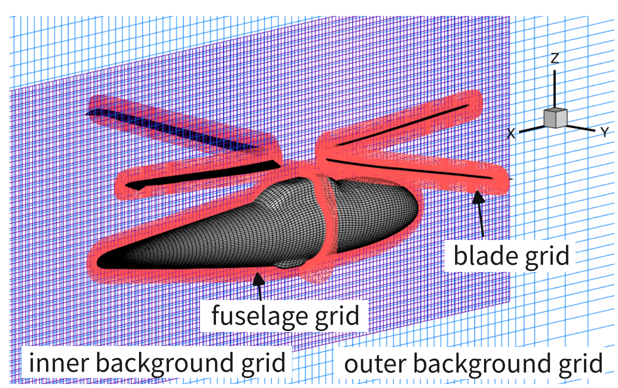

Figure 13: Computational grid

Focusing on the fluctuations of each coefficient shown in Figures 14 and 15, the thrust and torque fluctuations increase when aerodynamic deformation is considered. These discrepancies arise from differences in load distribution across the rotor disk, which are caused by changes in the effective angle of attack due to blade motions. Figure 16 shows that from 270° to 40° azimuth, the blade normal force increases in case 2 compared to case 1. Similarly, Figure 17 shows that from 270° to 45° azimuth, the blade drag force increases in case 2 compared to case 1. As shown in Figure 12, aeroelasticity causes a torsional deformation on the retracted side and an upward flapping motion at an azimuth of 300°. such blade motion reduces the effective angle of attack on the retreating side, thus reducing the flow separation on the retreating side (Figure 18). As a result, the blade normal force C_nM^2 and the blade drag C_qM^2 decrease mainly on the retreating side in case 1, and the rotor thrust force C_T and rotor torque coefficient C_Q decrease in case 2.

It is suggested that the method proposed in this paper can be used for the validation of CFD by comparing not only the aerodynamic coefficients but also other physical quantities such as pressure and velocity distributions measured in wind tunnel tests because the blade behavior can be reproduced in the CFD simulation.

CONCLUSIONS

In this paper, a method for reconstructing the aeroelastic deformation of a helicopter blade based on the deformation data measured by Model Deformation Measurement (MDM) is proposed and the detail of the method is introduced. CFD simulation was performed forcing the deformation shapes at arbitrary azimuth angles reconstructed by the proposed method, and the results were compared with the aerodynamic coefficients of the rotor obtained in wind tunnel tests. As a result, the following conclusions are obtained.

1. Comparing the MDM data with the reconstructed blade deformation shape using the proposed method, it is found that the deformed geometry identification can be performed with an error of about 0.3 mm.

2. Comparing the CFD results using the reconstructed deformed shape with those assuming the rigid blade reveals that certain differences in the vibration behavior of thrust and torque. Detailed investigation of the discrepancies, such as, through comparison with surface pressure data acquired during the experiment, could improve the CFD modeling accuracy.

Author contact: Kohei Konishi k-konishi@st.go.tuat.ac.jp

Table 4: Comparison of rotor performances

	Thrust Coeff. C_T	Torque Coeff. C_Q
Case 1	7.10×10^{-3}	3.86×10^{-4}
Case 2	7.44×10^{-3}	5.07×10^{-4}
WTT	7.31×10^{-3}	4.45×10^{-4}

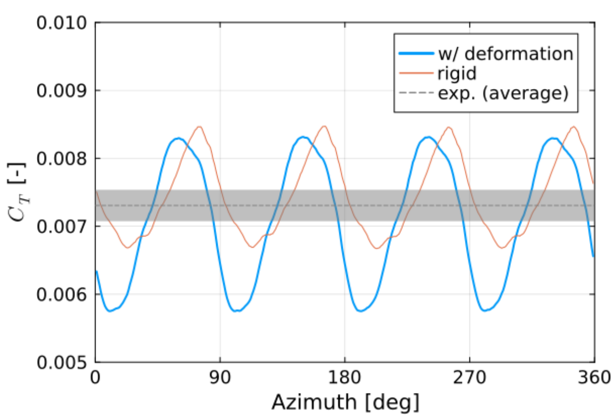

Figure 14: Rotor thrust coefficient C_T at each azimuth

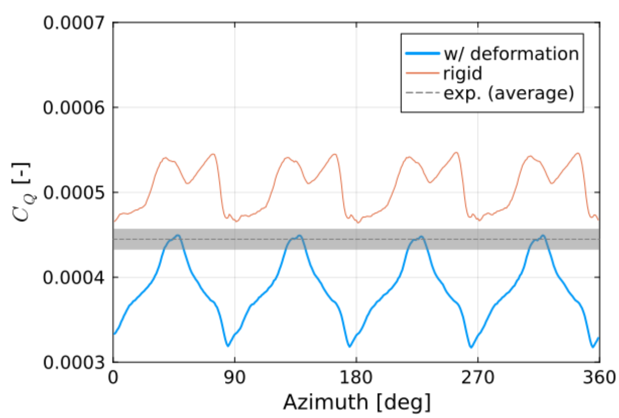

Figure 15: Rotor torque coefficient C_Q at each azimuth

ACKNOWLEDGMENTS

This research was supported by Japan Society for the Promotion of Science Grant-in-Aid for Scientific Research (KAKENHI) Grant Number 22H01396 and 23K22667, and supported by Japan Science and Technology Agency, JST SPRING, Grant Number JPMJSP2116. All numerical simulations presented in this paper was executed on the JAXA supercomputer system (JSS3).

REFERENCES

1. Mian, H. H., Wang, G., and Ye, Z.-Y., "Numerical investigation of structural geometric nonlinearity effect in high-aspect-ratio wing using CFD/CSD coupled approach," *Journal of Fluids and Structures*, Vol. 49, 2014, pp. 186–201.

2. Bhardwaj, M. K., Kapania, R. K., Reichenbach, E., and Guruswamy, G. P., "Computational Fluid Dynamics/Computational Structural Dynamics Interaction Methodology for Aircraft Wings," *AIAA Journal*, Vol. 36, (12), 1998, pp. 2179–2186.

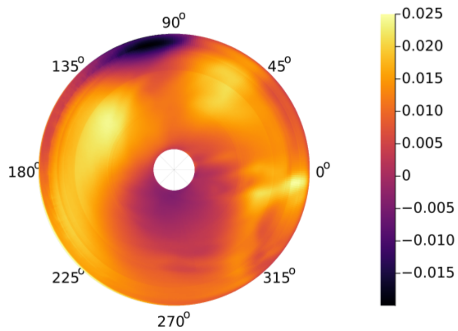

(a) Case 1

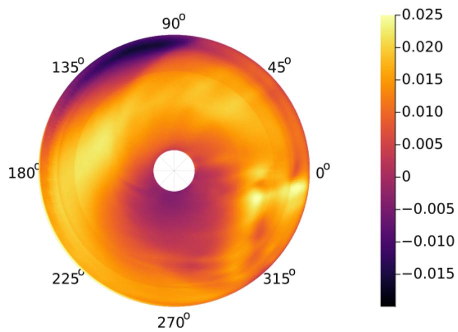

(b) Case 2

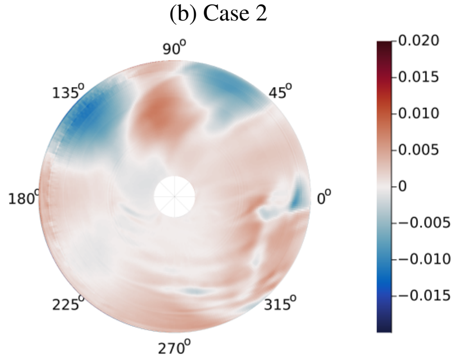

(c) Difference (Case1 − Case2)

Figure 16: Distribution of the blade normal force C_nM^2

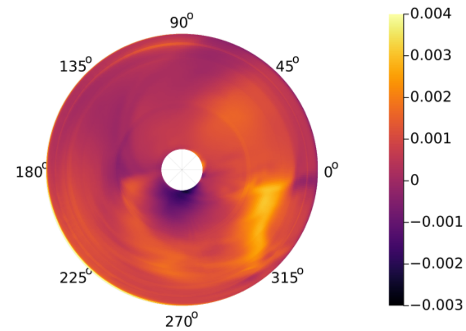

(a) Case 1

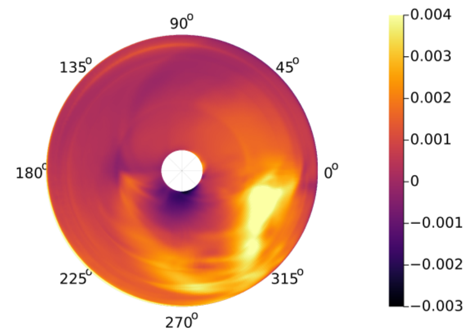

(b) Case 2

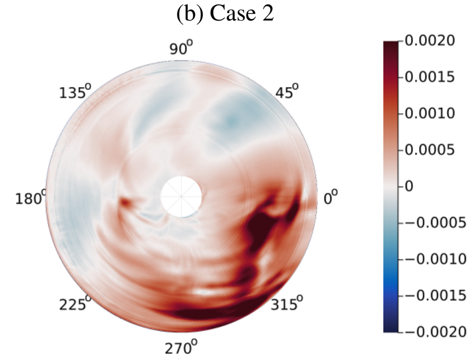

(c) Difference (Case1 − Case2)

Figure 17: Distribution of the blade drag C_qM^2

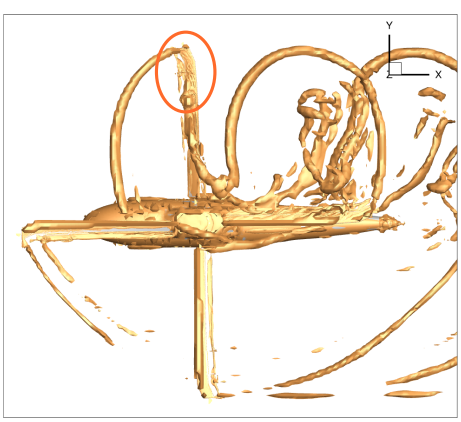

(a) Case 1

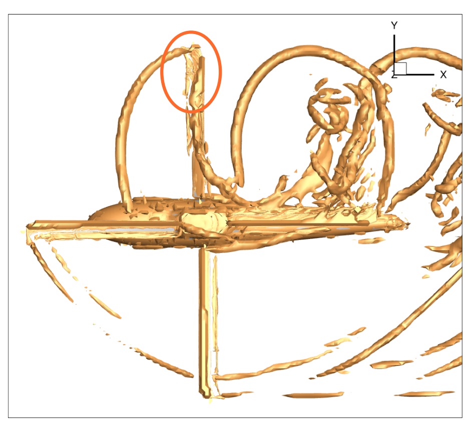

(b) Case 2

Figure 18: Visualization of blade vortex (iso-surface at Q = 0.1)

3. Smith, M. J., Lim, J. W., van der Wall, B. G., Baeder, J. D., Biedron, R. T., Boyd, D. D., Jayaraman, B., Jung, S. N., and Min, B.-Y., “The HART II international workshop: an assessment of the state of the art in CFD/CSD prediction,” *CEAS Aeronautical Journal*, Vol. 4, (4), Dec 2013, pp. 345–372. DOI: 10.1007/s13272-013-0078-8.

4. van der Wall, B. G., Lim, J. W., Riemenschneider, J., Kalow, S., Wilke, G. A., Boyd, D. D., Bailly, J., Delrieux, Y., Cafarelli, I., Tanabe, Y., Sugawara, H., Jung, S. N., Hong, S. H., Kim, D.-H., Kang, H. J., Barakos, G., and Steininger, R., “New smart twisting active rotor (STAR): pretest predictions,” *CEAS Aeronautical Journal*, Apr 2024.

5. Tinoco, E. N., Brodersen, O. P., Keye, S., Laflin, K. R., Feltrop, E., Vassberg, J. C., Mani, M., Rider, B., Wahls, R. A., Morrison, J. H., Hue, D., Roy, C. J., Mavriplis, D. J., and Murayama, M., “Summary Data from the Sixth AIAA CFD Drag Prediction Workshop: CRM Cases,” *Journal of Aircraft*, Vol. 55, (4), 2018, pp. 1352–1379.

6. Rumsey, C. L., Slotnick, J. P., and Sclafani, A. J., “Overview and Summary of the Third AIAA High Lift Prediction Workshop,” *Journal of Aircraft*, Vol. 56, (2), 2019, pp. 621–644.

7. Jung, S. N., You, Y. H., Dhadwal, M. K., Riemenschneider, J., and Hagerty, B. P., “Study on Blade Property Measurement and Its Influence on Air/Structural Loads,” *AIAA Journal*, Vol. 53, (11), 2015, pp. 3221–3232. DOI: 10.2514/1.J053686.

8. Meng, Y., Xie, C., An, C., Xu, Q., and Yang, C., “Three-dimensional large deformation reconstruction for slender wing-like structures from strain measurements,” *Measurement*, Vol. 204, 2022, pp. 111969.

9. Schneider, O., “Analysis of SPR measurements from HART II,” *Aerospace Science and Technology*, Vol. 9, (5), Rotorcraft Research, 2005, pp. 409–420.

10. Imai, M., Nakakita, K., and Kameda, M., “Random-dot pressure-sensitive paint for time-resolved measurement of deformation and surface pressure of transonic wing flutter,” *Experiments in Fluids*, 2023.

11. Yamamoto, S., and Daiguji, H., “Higher-order-accurate upwind schemes for solving the compressible Euler and Navier-Stokes equations,” *Computers & Fluids*, Vol. 22, (2), 1993, pp. 259–270. DOI: https://doi.org/10.1016/0045-7930(93)90058-H.

12. Tanabe, Y., and Saito, S., “Significance of All-Speed Scheme in Application to Rotorcraft CFD Simulations,” *The 3rd International Basic Research Conference on Rotorcraft Technology, Nanjing, China, 2009*, 2009.